Dislocations in diamond: Dissociation into partials and their glide motion

A. T. Blumenau*
School of Physics, University of Exeter, Exeter EX4 4QL, United Kingdom
and Department of Physics, Universität Paderborn, D-33098 Paderborn, Germany

R. Jones
School of Physics, University of Exeter, Exeter EX4 4QL, United Kingdom

T. Frauenheim
Department of Physics, Universität Paderborn, D-33098 Paderborn, Germany

B. Willems, O. I. Lebedev, and G. Van Tendeloo
Department of Physics-EMAT, University of Antwerp (RUCA), B-2020 Antwerp, Belgium

D. Fisher and P. M. Martineau
DTC Research Centre, Belmont Road, Maidenhead, Berkshire SL6 6JW, United Kingdom
(Received 16 August 2002; revised manuscript received 3 February 2003; published 30 July 2003)

The dissociation of 60° and screw dislocations in diamond is modeled in an approach combining isotropic elasticity theory with *ab initio*–based tight-binding total-energy calculations. Both dislocations are found to dissociate with a substantial lowering of their line energies. For the 60° dislocation, however, an energy barrier to dissociation is found. We investigate the core structure of a screw dislocation distinguishing ''shuffle,'' ''mixed,'' and ''glide'' cores. The latter is found to be the most stable undissociated screw dislocation. Further, the glide motion of 90° and 30° partials is discussed in terms of a process involving the thermal formation and subsequent migration of kinks along the dislocation line. The calculated activation barriers to dislocation motion show that the 30° partial is less mobile than the 90° partial. Finally, high-resolution electron microscopy is performed on high-temperature, high-pressure annealed natural brown diamond, allowing the core regions of 60° dislocations to be imaged. The majority of dislocations are found to be dissociated. However, in some cases, undissociated 60° dislocations were also observed.

DOI: 10.1103/PhysRevB.68.014115 PACS number(s): 61.72.−y, 61.72.Lk, 61.72.Bb, 68.37.Lp

I. INTRODUCTION

Dislocations are very common defects in both natural as well as chemical vapor deposition (CVD)–grown diamond: Natural gem-quality type Ia diamond is almost dislocation-free[1] but type II usually contains a considerable amount of dislocations. For type IIa, for example, densities as high as 10^7 cm^{-2} have been reported.[2–4] CVD-grown polycrystalline diamond has been found to contain very high dislocation densities of 10^{12} cm^{-2}. Some of these dislocations lie at or near grain boundaries[5] while others originate at the substrate interface and propagate through the thin film.[6]

The main slip system in diamond has been experimentally confirmed to be the $\{111\}\langle 110\rangle$ type,[7–10] where dislocations lie on $\{111\}$ planes and possess $\langle 110\rangle$ Burgers vectors. Further, weak-beam electron microscopy revealed that dislocations in type IIa diamond were dissociated into $\frac{1}{2}[1\bar{1}0]$ glide partials separated by an intrinsic stacking fault of width 25–42 Å. Also, many extended dislocation nodes and dipoles consisting of edge and 60° dislocations were observed.

While earlier *ab initio* studies of dislocations in diamond were limited to the analysis of the structure and energetics of 90° partial glide dislocations,[11–13] we recently presented a systematic study of the low-energy core structures of perfect and partial dislocations in the $\{111\}\langle 110\rangle$ slip system.[14] Moreover, the electronic structures of these dislocations were found and compared with experimental electron energy-loss spectra.[15] Glide partial dislocations were generally found to be electrically inactive. However, shuffle dislocations, or alternatively point-defects, which possess states in the electronic band gap, might be responsible for the band-*A* cathodoluminescence linked to dislocations in natural type IIa diamond at 2.8–2.9 eV[2,3,16,17] or even for the brown coloring common to many natural diamonds.[18]

The remaining question revolves around the dissociation of perfect dislocations in diamond and the movement of dislocations. In our previous study we calculated the dissociation widths of screw and 60° dislocations, finding values around 30 and 35 Å, respectively. It was also possible to rule out certain dissociation reactions by just comparing the core energies of isolated dislocations.[14] However, the full energetics could not be described in that simple approach and in Sec. III, we reexamine the dissociation of the screw and the 60° glide dislocation. In this context a more detailed investigation of the $\frac{1}{2}[1\bar{1}0]$ screw became necessary, which had only been discussed in its shuffle structure.[14] This is followed by a discussion on the movement of the partial dislocations and calculate both the formation energies of kinks and their migration barriers. Finally, in Sec. IV we present the first, to the best of our knowledge, high-resolution electron microscopy images of dislocation cores in

diamond. The lattice images reveal dissociation of both 60° and screw dislocations, although some of the latter remain undissociated.

II. COMPUTATIONAL METHOD

Continuum elasticity theory supposes that atomic displacements vary slowly over the dimensions of a defect and thus fails to address properly the properties of the dislocation core, where the atomic displacements are considerable. To model this region, and remove the uncertainty implicit in the use of empirical potentials, a first-principles electronic structure method is to be preferred. In this work we use a **d**ensity-**f**unctional-based **t**ight-**b**inding approach (DFTB). Here the electronic wave functions are approximated by a linear combination of atomic orbitals involving a minimal basis set of *s* and *p* orbitals. The two center Hamiltonian and overlap matrix elements result from atom-centered valence electron orbitals and the atomic potentials from single-atom calculations in **d**ensity **f**unctional **t**heory (DFT). Exchange and correlation contributions in the total energy as well as the ionic core-core repulsion are taken into account by a repulsive pair potential. The latter is obtained by comparison with DFT calculations. Thus the DFTB method can be seen as an approximate density functional scheme.[19,20] In this work, the structures are geometrically optimized using a conjugate gradient algorithm until all forces are well below 5×10^{-3} eV/Å.

Recently, the DFTB method has been applied to model dislocation core structures and energies in diamond[14,15] and was found to give results in good agreement with DFT pseudopotential calculations (AIMPRO[21,22]). Also, excellent agreement was found with other DFT calculations[13] carried out on the 90° glide partial dislocation in diamond.

As stated in Ref. 14, DFTB overestimates the elastic constants when compared with experimental values. Applying the Voigt averaging procedure[9] results in a shear modulus of $\mu = 554$ GPa (3% too large) and a Poisson's ratio $\nu = 0.088$ (29% too large). The gross error in the latter is not regarded as a serious objection to DFTB as expressions for the energy usually involve $1 \pm n\nu$ where n is 1 or 2 (see Hirth and Lothe[9] for expressions for dislocation energy factors and interaction forces between dislocations and between kinks). Consequently, the large error for the Poisson's ratio has no appreciable effect on the energies of defects reported here.

III. THEORETICAL RESULTS AND DISCUSSION

We previously[14] investigated the structure and the energetics of the shuffle screw dislocation. However, the shuffle screw dislocation is a metastable defect and cannot dissociate without overcoming an energy barrier. It is apparent that there is more than one type of screw dislocation and before discussing the energetics for dissociation in greater details, it is necessary to describe the different structures and energies of the undissociated screw dislocation.

A. The $\frac{1}{2}[1\bar{1}0]$ screw dislocation

To analyze the isolated straight screw dislocation in diamond, the supercell-cluster hybrid model, as described in Ref. 14 is used. The model contains a single dislocation segment which is repeated periodically along the dislocation line. Surrounding the core is a cylinder of bulk diamond terminated by hydrogenated surfaces. This hydrogenation does not represent a real physical presence, but is meant to suppress reconstruction and electrical activity of the surface, hence giving a better approximation to bulk material. We showed previously that clusters containing around 600 atoms with single or double periodicity along the dislocation line were sufficiently large to reproduce the asymptotic strain energy given by elasticity theory.

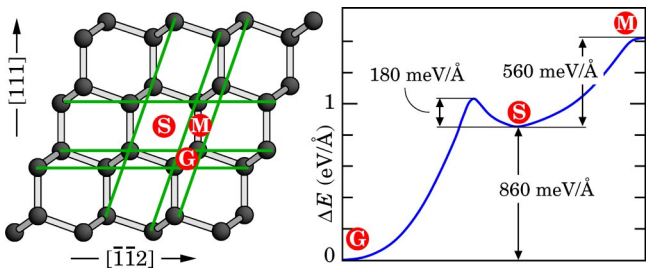

FIG. 1. The three types of the $\frac{1}{2}[1\bar{1}0]$ screw dislocation: Shuffle, glide and mixed (labeled **S**, **G**, and **M**, respectively). *Left:* The core positions projected into the $(1\bar{1}0)$ plane. The two sets of $\{111\}$ planes containing the line direction are indicated. *Right:* Relative core energies of the three different types and barriers between them. The x axis gives a parameter for transformation **G** $\rightarrow$**S**$\rightarrow$**M** (see text for further details).

To obtain an initial structure for the screw dislocation, the atoms of a hybrid model, as described above, are displaced with respect to their positions in a perfect lattice.[33] However, several structures are possible, depending on the origin of the radial symmetric displacement field. All of these represent different screw dislocations which can transform into each other without the need of vacancies or interstitials. One can distinguish between shuffle and glide in a similar way as in the case of the perfect 60° dislocation. For a $\frac{1}{2}[1\bar{1}0]$ screw dislocation there are two sets of $\{111\}$ planes containing its line direction. Hence, in terms of shuffle and glide, there are three possible unique types as illustrated in Fig. 1 (left): Shuffle, glide, and mixed. The first two have shuffle, or respectively, glide character with respect to both the horizontal and the inclined set of $\{111\}$ planes, whereas the mixed type has shuffle character with respect to one and glide character with respect to the other set of $\{111\}$ planes.

a. Core structures. The relaxed structures of the three types of the screw dislocation can be found in Fig. 2. The bond angles and lengths near the core of the shuffle structure are stretched but all bonds are bulklike and all atoms remain fourfold coordinated. This is a result of the origin of the displacement field avoiding any bonds or atoms. The situation is very different for the glide screw and for the mixed screw, where the origins lie exactly on a row of bonds [see Fig. 1 (left)]. As a result, the two neighboring atoms (**A** and **B** in Fig. 2) connected by one of those bonds are displaced with respect to each other by half the Burgers vector along $[1\bar{1}0]$.

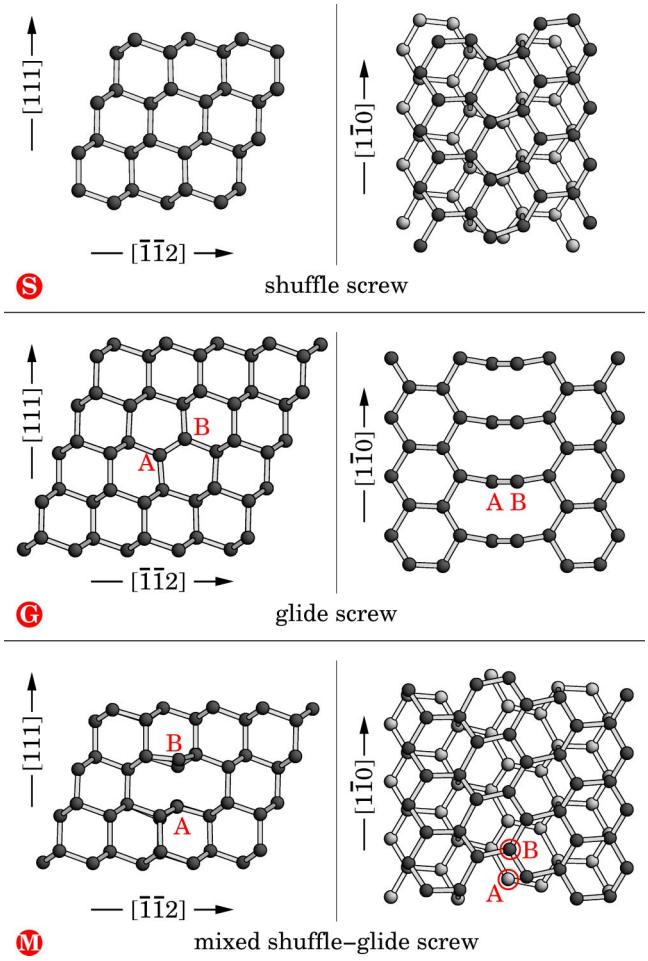

FIG. 2. The relaxed core structures of the three basic types of $\frac{1}{2}[1\bar{1}0]$ screw dislocations (compare with Fig. 1). For each structure the *left* figure gives the projection into the $(1\bar{1}0)$ plane and the *right* figure the projection into the (111) plane. *Upper panel:* The shuffle screw. In the [111] projection (*right*) two (111) planes are shown, the lower one is drawn in light gray. *Middle panel:* The glide screw. Atoms **A** and **B** (and equivalent atoms along $[1\bar{1}0]$) are only threefold coordinated. *Lower panel:* The mixed-type screw. Again, in the [111] projection (*right*) two (111) planes are shown, the lower one is drawn in light gray. The distance between Atoms **A** and **B** (and equivalent atoms along $[1\bar{1}0]$) is too large for bonds to be formed.

In case of the glide screw this leads to a planar sp^2 bonding situation for both atoms **A** and **B** which are separated by 0.90 Å. Subsequent structural relaxation pushes the two atoms apart, resulting in an appreciable C-C bond length of 1.33 Å. The relaxed structure is basically that of two 30° partial glide dislocations in the same Peierls valley. However, there is no bond reconstruction along the dislocation line.

For the mixed-type screw dislocation, the two atoms closest to the origin of the displacement (**A** and **B** in Fig. 2) are widely separated in the $[1\bar{1}0]$ projection. Thus, after displacement, their distance is large enough to break the connecting bond. Subsequent relaxation does *not* lead to a bond reconstruction. The mixed structure was suggested by Koizumi *et al.*,[23] and for III-V compound semiconductors the same authors claim it to be more stable than the shuffle structure.

b. Energetics and stability. To model the transformation from **M**→**S** and **G**→**S** and to scan for barriers between them, the two atoms adjacent to **M**, or respectively, **G** are constrained parallel to the $(1\bar{1}0)$ plane, preventing relaxation to a stable or metastable position. In Fig. 2 these atoms are labeled **A** and **B**, a different pair for **M**→**S** and **G**→**S**, respectively. The $[1\bar{1}0]$ projected distance between **A** and **B** defines the configuration coordinate used in Fig. 1 (right). The curve represents about 20 grid points for **G**→**S** and 10 grid points for **S**→**M**, interpolated by a spline. When modeling transformation **M**→**S** and **G**→**S**, the surface of the supercell-cluster hybrid is maintained. Hence, if in structure **S** the dislocation core is centered with respect to the surface, then in **M** it will be slightly off center. Fortunately, this symmetry breaking has only a small effect on the total energy: Test calculations give an energy lowering of <80 meV/Å if a screw dislocation is displaced along a full lattice translation away from the center. As both transformations **M**→**S** and **G**→**S** involve only half a lattice translation, the effect on the energy will be much smaller.

The glide screw appears to be the lowest-energy structure and is chosen as energy zero in Fig. 1. The shuffle screw has a $\sim$860 meV/Å higher core energy, which is, however at, least metastable with a barrier of $\sim$180 meV/Å. Finally the mixed type exceeds the shuffle type by $\sim$560 meV/Å. The latter structure is unstable and represents a saddle point between two adjacent sites of the shuffle core.

B. Dissociation into 30° and 90° partials

As discussed in Ref. 14, the screw dislocation can dissociate into two 30° glide partial dislocations and the 60° glide dislocation can dissociate into a 30° and a 90° glide partial. In both cases the pair of partials is separated by an intrinsic stacking fault. Since the structures and core energies of the 60° glide and of the partial dislocations have been presented in detail previously, they will not be repeated here. It has only to be noted that the 90° glide partial exists in both a single-period and double-period core reconstruction, with the latter possessing a lower energy. For reasons of simplicity, however, in this work we will only consider the single-period core structure explicitly and then extrapolate for the double-period core whenever possible.

a. The dissociation energy in the elastic limit. When it comes to the dissociation of perfect dislocations into Shockley partials, the two competing energy contributions in the elastic limit are the stacking fault energy and the elastic partial-partial interaction energy. The former grows proportionally with partial-partial separation R: $E_{\mathrm{ISF}}/L=\gamma R$ gives the energy per unit length. In an infinite and isotropic crystal the interaction energy of two straight and parallel dislocations A and B of arbitrary Burgers vectors $\boldsymbol{b}_{\mathrm{A}}$ and $\boldsymbol{b}_{\mathrm{B}}$ and line direction ℓ is given as:

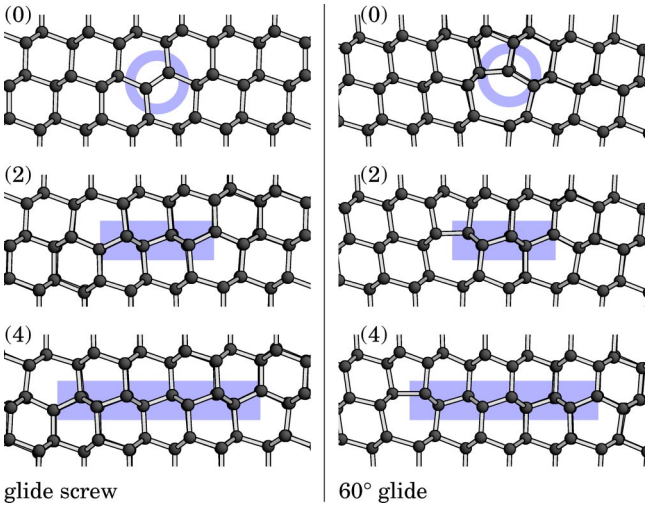

FIG. 3. The first stages of dissociation of the glide screw and the 60° glide dislocation. The view is projected into the $(1\bar{1}0)$ plane. The top structure labeled (**0**) shows the respective undissociated perfect dislocation. The stacking fault in the second (**2**) and fourth (**4**) dissociation step is shaded. *Left:* The dissociation of the $\frac{1}{2}[1\bar{1}0]$ glide screw into two 30° glide partials. *Right:* The dissociation of the 60° glide dislocation into a single-period 90° glide and a 30° glide partial.

$$\frac{E_{\rm int}(\boldsymbol{R})}{L} = -\frac{\mu}{2\pi}\left\{(\boldsymbol{b}_{\rm A}\cdot\boldsymbol{\ell})(\boldsymbol{b}_{\rm B}\cdot\boldsymbol{\ell}) + \frac{(\boldsymbol{b}_{\rm A}\times\boldsymbol{\ell})\cdot(\boldsymbol{b}_{\rm B}\times\boldsymbol{\ell})}{1-\nu}\right\}\ln\left(\frac{R}{R_0}\right) - \frac{\mu}{2\pi(1-\nu)R^2}[(\boldsymbol{b}_{\rm A}\times\boldsymbol{\ell})\cdot\boldsymbol{R}][(\boldsymbol{b}_{\rm B}\times\boldsymbol{\ell})\cdot\boldsymbol{R}]. \quad (1)$$

Here $\boldsymbol{R}$ is the distance vector between the two dislocations. Equation (1), which was first developed by Nabarro,[24] allows the calculation of the interaction energy except for an energy shift $\propto\ln(R_0/\text{Å})$. This shift cannot be determined in linear elasticity theory.

When a perfect dislocation dissociates, the two partials usually reside in the same glide plane and the term proportional to R^{-2} in Eq. (1) vanishes. The interaction energy then simply varies logarithmically with R.

b. Atomistic modeling. Dissociation of a perfect dislocation into two partials bordering a stacking fault creates a defect whose core is considerably extended within the glide plane. It is not possible to describe this structure as a single defect without constraining the stacking fault ribbon. Here, we use hybrid cluster models with about 700 atoms containing the two partials separated by up to 8.75 Å corresponding to four lattice translations along $[\bar{1}12]$. The distances between the surface H atoms and the cores is then 9.5 Å. Figure 3 shows the relaxed geometries for the undissociated screw and 60° glide dislocation, as well as the second and also the fourth dissociation step leading to wider stacking faults. The corresponding relative energies are given in Fig. 4.

Now, with the atomistic results at hand, the unknown energy offset $\propto\ln(R_0/\text{Å})$ of elastic interaction energy $E_{\rm int}/L$ in Eq. (1) can be found easily by adjusting $E_{\rm int}/L+E_{\rm ISF}/L$ to the atomistic DFTB energy at the fourth dissociation step. In this calculation, we take shear modulus μ, Poisson's ratio ν, and stacking fault energy γ to be 554 GPa, 0.088, and 293 mJ/m^2, respectively. These are the values found with the DFTB method.[14] This procedure yields $R_0=1.7$ and 4.4 Å for the screw and 60° dislocation, respectively. In Fig. 4, the resulting energies deduced from Eq. (1) and the stacking fault energy are drawn as solid lines for both dislocation types and allow an extrapolation to larger stacking fault widths. One can observe that the atomistic calculation and continuum theory still agree well for the third stage of dissociation. For smaller stacking fault widths lying in the region of overlapping dislocation core radii, however, the deviation becomes obvious and finally, as $R\to 0$, the continuum result diverges.

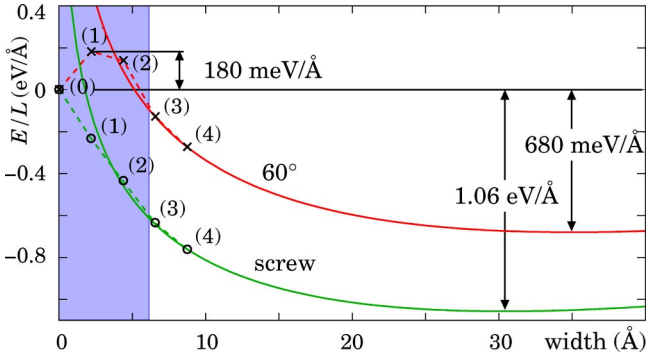

FIG. 4. The dissociation energy of the glide screw and the 60° glide dislocation. The relative atomistic density-functional-based tight-binding energies of the first four dissociation steps and of the undissociated dislocation are labeled (**1**) to (**4**) and (**0**), respectively. Zero energy is set to the undissociated dislocations. The solid lines represent the sum of the stacking fault energy and the elastic interaction energy as given in continuum theory [Eq. (1)]. The shaded region, ~6 Å, indicates where the two core radii of the respective partial dislocations overlap—the region where continuum elasticity theory fails.

Both for the screw and 60° dislocation, the final dissociation energy at equilibrium separation between the partials is clearly below the energy of the undissociated dislocation (-1.06 eV/Å and -0.680 eV/Å, respectively). Hence, dissociation into partial dislocations is strongly favored on energetic grounds.

A striking difference between the dissociation of the two types of dislocations is the presence of an energy barrier of ~180 meV/Å to initiate dissociation of the 60° dislocation, whereas for the screw there is no such barrier. It should be noted, however, that barriers, which are not shown in Fig. 4, must separate each structure denoted by (**0**), (**1**) to (**4**), else these structures would be unstable. In fact, the energies given refer to structures corresponding to local minima where the dislocations occupy Peierls valleys. Each dissociation step requires a barrier to be overcome and a high temperature and/or high stress is then required to move the partial dislocation. This thermal motion of the glide partials will be considered in the following section.

Finally, in the case of the dissociation of the 60° glide dislocation, only the single-period 90° partial was considered. The energy of the respective systems containing a

double-period 90° instead would be approximately 170 meV/Å lower, as given by the differences in core energies.[14]

C. Dislocation glide motion

Dislocation glide arises from stress derived from external forces on the crystal or, as discussed in the last section, from the interaction with neighboring dislocations. When the stress is insufficient to overcome the Peierls barrier, kinks must be generated by a thermal process and motion occurs by their migration along the dislocation line. Since kinks on a dislocation line can only be created in pairs, their density in thermodynamic equilibrium is controlled by double-kink formation energy $2E_f$, whereas their rate of motion depends on kink migration barrier W_m. In the case when obstacles such as point defects and impurities are not present, and for short dislocation segments, the activation energy for glide motion Q is then given as the sum of $2E_f$ and W_m. One obtains for the glide velocity:[9]

$$v_{\mathrm{disl}} \propto e^{-Q/(kT)} \quad \text{with} \quad Q = 2E_f + W_m. \tag{2}$$

For long dislocation segments, however, the activation energy is controlled by the sum of single-kink formation energy E_f and kink migration barrier.[9]

In the following, the two crucial parameters E_f and W_m for the 30° and the 90° partial will be found. The energetics of reconstruction phase defects, as discussed in the context of dislocation glide in silicon in Refs. 25,26 will not be considered.

1. Kink formation and migration at the 90° partial

a. Kink formation. The analysis of the formation and migration of kinks was carried out using a hydrogenated cluster $C_{420}H_{214}$. This avoids the effect of kink-kink interaction in periodic cells although, of course, there is then an interaction with the cluster surface. For the 90° glide partial, this cluster extends six lattice translations along the dislocation line and allows double kinks with a kink-kink separation of two lattice translations ($\sqrt{2}\,a_0$ with a_0 as the lattice parameter) to be investigated. The nearest distance of the kink with the surface is then $\sqrt{2}\,a_0$.

Figure 5 (top left) shows projection onto a section of the (111) glide plane containing a relaxed and reconstructed kink at the single-period 90° partial. All atoms are fourfold coordinated and the stacking fault is shaded. The structures of the left kink (LK) and the right kink (RK) are identical. The formation energy of the kink pair, with separation $L = \sqrt{2}\,a_0$, is obtained as the difference in total DFTB energy between the fully relaxed model containing the kinked and one of the same stoichiometry and geometry containing the unkinked dislocation segment. No surface constraints are used. The calculation yields a formation energy of $E_{\mathrm{pair}}(L = \sqrt{2}\,a_0) = 1.0$ eV.

Assuming the formation energy of a single left kink and a single right kink to be the same E_f, and including the energy of the faulted region generated together with the kinks, one obtains:

$$2E_f = E_{\mathrm{pair}}(L) - E_{\mathrm{KK}}(L) - aL\gamma. \tag{3}$$

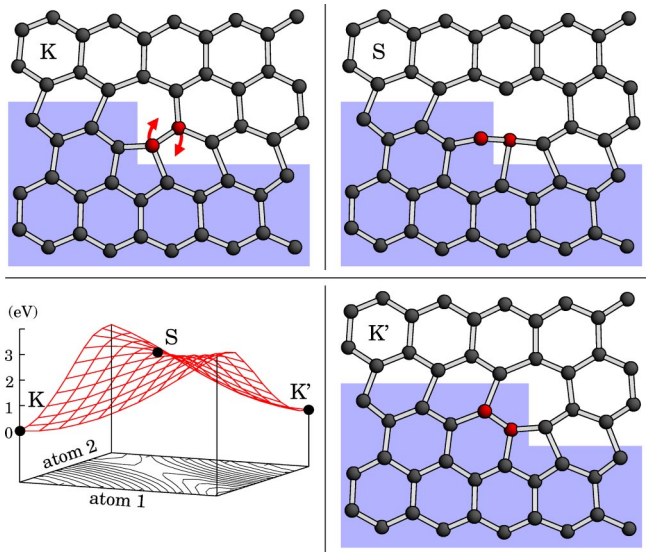

FIG. 5. Kink migration at the single-period 90° glide partial. The three main stages of one elementary kink migration step are illustrated: The relaxed structures of starting kink **K**, saddle point **S**, and migrated kink **K′** are shown projected into the glide plane. The faulted region is shaded and arrows indicate the motion of the two involved atoms. *Lower left panel:* The parameterized energy surface of the corresponding process leading from **K** via **S** to **K′**. The two parameters are defined via the projected coordinates of the two involved moving atoms (see text).

Here a is the kink height and $E_{\mathrm{KK}}(L)$ the elastic kink-kink interaction energy given as:[9]

$$E_{\mathrm{KK}}(L) = -\frac{\mu a^2}{8\pi L(1-\nu)}\{|\boldsymbol{b}\cdot\boldsymbol{\ell}|^2(1+\nu) + |\boldsymbol{b}\times\boldsymbol{\ell}|^2(1-2\nu)\}. \tag{4}$$

For the 90° partial, one obtains:

$$E_{\mathrm{KK}}(L) = -\frac{\mu a^2}{8\pi L}\frac{1-2\nu}{1-\nu}|\boldsymbol{b}_{90}|^2. \tag{5}$$

With a kink height $a = \sqrt{3/8}\,a_0$ corresponding to the separation of Peierls valleys, the single-kink formation energy E_f is 520 meV. For the particular kink-kink separation investigated, the elastic interaction and the contribution of the stacking fault nearly cancel each other.

b. Kink migration. To model kink migration along the dislocation line, the elementary migration step has to be parametrized so that the minimum-energy path leading from the starting to the final structure can be found and the barrier determined. Fortunately, all kink migration steps discussed in this work involve mainly the motion of two atoms which break bonds with neighboring atoms and form new bonds in the migration process. All other atoms remain at their respective lattice sites. For a right kink at the 90° partial, this is illustrated in Fig. 5. To find the intermediate saddle point structure **S**, the elementary kink migration step was parametrized by the coordinates of each of the two core atoms at the end of the kink projected onto the connect-

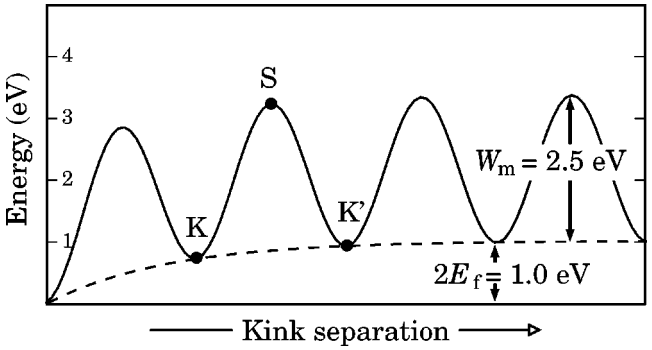

FIG. 6. Schematic representation of the energy of the glide process for the single-period 90° glide partial: A kink pair is formed and subsequent migration of the two kinks enlarges their separation. **K**, **S**, and **K′** are labeled for an arbitrary migration step. The dashed line connecting the minima represents the formation energy of the kink pair. The energy contribution of the expanding stacking fault is not included in the graph.

ing line between their initial and final positions. Varying these two parameters independently yields a two-dimensional energy surface, as shown in Fig. 5 (lower left panel).[34]

This procedure was applied to a cluster containing a dislocation segment with a single right kink, as well to one with a single left kink. The migration barrier appears to be $W_m = 2.5$ eV for both.

c. Glide motion of the 90° partial. With the kink migration barrier as well as the formation energy now at hand, the activation energy in the kink migration process evaluates to $Q_{90} \approx 3.5$ eV for short dislocation segments, following Eq. (2), and 3.0 eV for long segments. The energy corresponding to the whole glide process of the single-period 90° glide partial is schematically shown in Fig. 6. The first few minima are considerably lower due to the attractive kink-kink interaction.

Since the elementary processes are the same for kink migration along the double-period 90° glide partial, a similar barrier and formation energy can be expected.

2. Kink formation and migration at the 30° partial

This partial adopts a double-period reconstruction.[14] Hence, the situation is more complex and several different kink structures are involved.

a. Kink formation. Depending on the kink position relative to the reconstructed bonds along the core of the 30° partial, two different structures for the left kink as well as for the right kink are possible. These different structures will be labeled LK1 and LK2 and RK1 and RK2, respectively. Figure 7 shows sections of the (111) glide plane containing the relaxed and the reconstructed kink structures. As in the case of the 90° partial, for each kink all atoms are fourfold coordinated. To obtain the kink formation energies, clusters similar to those for the 90° partial are used. However, unlike the 90° partial, the structures of left and right kinks are very different and therefore, a similar formation energy cannot be expected. Now, in a cluster the formation energy of a single kink cannot be determined and it is only possible to obtain the sum of the two formation energies similar to Eq. (3):

$$E_f(\mathrm{LK}X) + E_f(\mathrm{RK}Y) = E_{\mathrm{pair}}(X,Y,L) - E_{\mathrm{KK}}(L) - aL\gamma. \tag{6}$$

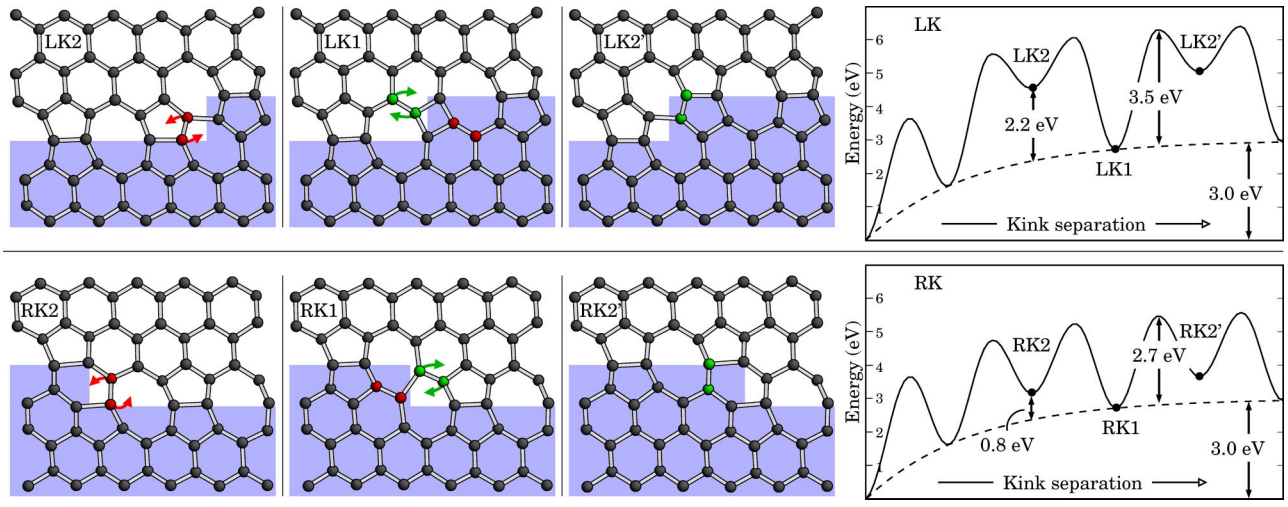

FIG. 7. Kink migration at the 30° glide partial. *Upper panel:* The elementary kink migration steps of the left kink LK2→LK1→LK2′. The relaxed structures of a starting kink **LK2**, and the subsequent kinks **LK1** and **LK2′** are shown projected into the glide plane. The saddle point structures are not given. The faulted region is shaded and arrows indicate the motion of the two involved atoms. *Lower panel:* The elementary kink migration steps of the right kink RK2→RK1→RK2′. *Right upper and lower panels:* On the far right a schematic representation of the energy of the glide process is given: A kink pair is formed and subsequent migration of the two kinks enlarges their separation. Since for the 30° partial the migration barriers differ for left and right kinks, the corresponding processes are shown separately. The dashed line connecting the minima represents the formation energy of the respective lowest energy kink pair. The energy contribution of the expanding stacking fault is not included.

X and Y can be 1 or 2 (compare Fig. 7). For the 30° partial the elastic kink-kink interaction energy evaluates as [Eq. (4)]:

$$E_{\mathrm{KK}}(L) = -\frac{\mu a^2}{32\pi L}\frac{4+\nu}{1-\nu}|\boldsymbol{b}_{30}|^2. \tag{7}$$

The formation energies of all possible four combinations (LKX,RKY) yields:

(1) $E_{\mathrm{f}}(\mathrm{LK1}) + E_{\mathrm{f}}(\mathrm{RK1}) = 3.0$ eV.
(2) $E_{\mathrm{f}}(\mathrm{LK2}) = E_{\mathrm{f}}(\mathrm{LK1}) + 2.2$ eV.
(3) $E_{\mathrm{f}}(\mathrm{RK2}) = E_{\mathrm{f}}(\mathrm{RK1}) + 0.8$ eV.

LK1 and RK1 are the lowest-energy kinks. Thus, in the kink migration process it is an LK1-RK1 double kink that will be preferentially formed at the initial stage. However, subsequent migration inevitably involves the two high-energy kinks as intermediate structures.

b. Kink migration. As a consequence of four different kink structures being involved, four migration barriers have to be determined. The corresponding migration steps LK2→LK1 →LK2′ and RK2→RK1→RK2′ are shown in Fig. 7. As one can see, LK2→ LK1 is just the reverse process of LK1→LK2′ since all involved structures are symmetric within the glide plane if the different stacking on either side of the dislocation is ignored. The same holds for RK2 →RK1 and RK1→RK2′. As expected, the two barriers for left kink migration are found identical within 1% error and so are the two right kink barriers:

(1) $W_{\mathrm{m}}(\mathrm{LK}) = 3.5$ eV.
(2) $W_{\mathrm{m}}(\mathrm{RK}) = 2.7$ eV.

b. Glide motion of the 30° partial. Figure 7 shows the resulting energy of the glide process at the 30° partial for an itinerant right and left kink separately. The physical picture mirrors that of the 90° partial. However, the existence of two different barriers for left and right kink migration results in a modified expression for the partial velocity. Equation (2) is replaced by:[26]

$$v_{\mathrm{disl}} \propto e^{-[E_{\mathrm{f}}(\mathrm{LK1})+E_{\mathrm{f}}(\mathrm{RK1})]/kT}\left[e^{-[W_{\mathrm{m}}(\mathrm{LK})]/kT} + e^{-[W_{\mathrm{m}}(\mathrm{RK})]/kT}\right]. \tag{8}$$

Due to its lower migration barrier, the right kink is more mobile than the left kink and dominates the partial velocity. However, unlike in the case of the 90° partial, where the migration barriers clearly control the velocity, here the rather high kink formation energy plays an almost equal role.

The arithmetic mean of the activation barriers for right and left kink formation and migration evaluates as $\overline{Q}_{30} \approx 6.1$ eV for short dislocation segments. The 90° partial appears to be the by far more mobile partial dislocation. The stacking fault width will then increase if the mobile partial leads, increasing the back stress on the leading partial and hence slowing it down. The reverse happens if the mobile partial trails.

3. Comparison with independent theoretical work

Similar atomistic calculations of kink formation energies and mobilities have been carried out in Ref. 26 for silicon only, and thus cannot be compared directly. The structures found for silicon are very similar to those found for diamond in this work. However, formation energies and barriers appear to be considerably lower in silicon than they are in diamond, which reflects the hardness of diamond. Also, for silicon the left kinks appear to be the more mobile species at the 30° partial.

For the 90° partial in diamond, theoretical results for the activation barrier Q_{90} vary between 2.9 eV for a soliton mechanism as described in Ref. 27 and 3.3 eV in Ref. 11, both lower than the 3.5 eV found here.

IV. HIGH-RESOLUTION ELECTRON MICROSCOPY

A. Sample preparation and experimental setup

Several samples of brown natural type IIa diamond were treated at different temperatures with diamond stabilizing pressures [i.e., high-pressure, high-temperature (HPHT) annealing]. Diamond slabs with dimensions of approximately 2 mm×2 mm×100 μm were produced for TEM specimens by laser cutting and subsequently thinned by ion-beam milling to electron transparency.

We applied high-resolution electron microscopy (HREM) to these samples to resolve the atomic core structures of dislocations. For HREM, a JEOL 4000EX microscope with a Scherzer resolution of 0.17 nm was used. All samples were oriented with the ⟨011⟩ axis parallel to the electron beam. For the interpretation of HREM observations it is necessary to have the dislocation line as close as possible to the [110] viewing direction. When the dislocation line lies locally along the [110] direction, the in-plane strain field around the dislocation line is approximately symmetrical. The contrast produced in these HREM images enables us to resolve the atomic structure of the dislocation core and to compare these experimental images with the theoretically calculated dislocation core structures.[28]

B. Results

Experimental evidence of dissociated 60° dislocations in type IIa diamond has been given earlier by Pirouz *et al.*[10] using weak-beam TEM. In the same work the stacking fault energy was determined. Previous HREM work mainly focused on various defect structures such as dislocations, stacking faults, and twins and grain boundaries in thin films of synthetic diamonds.[29–32] In this context, the stacking fault energy was determined by deducing the ribbon width from HREM observations of dissociated 60° and screw dislocations in synthetic diamond.[28]

Our plan-view HREM images show 60° dislocations in plastically deformed natural type IIa brown diamonds after HPHT annealing. With our investigation limited to line directions along ⟨110⟩, mainly dissociated 60° dislocations are observed.

Figure 8 depicts a HREM image of a 60° dislocation dissociated into a 90° and 30° partial. The two partials border

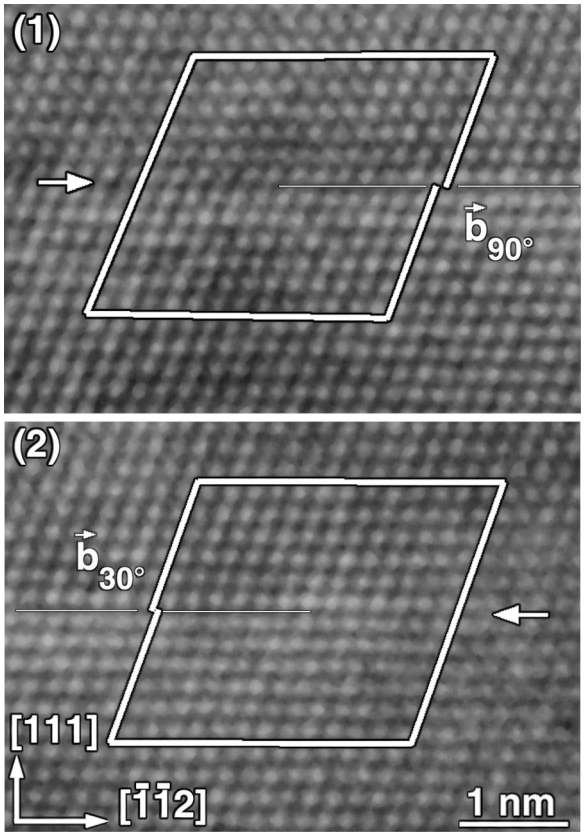

FIG. 8. Plan-view high-resolution electron microscopy image of a dissociated 60° dislocation into a 90° (a) and a 30° partial (b) in plastically deformed type IIa diamond after high-pressure, high-temperature annealing. The Burgers circuits are drawn for both partial dislocations. The glide partials border the same stacking fault ribbon, whose plane is marked by an arrow and a thin white line. Burgers vectors of the glide partials are also indicated near the Burgers circuits.

the same stacking fault which is marked by an arrow in both figures. A Burgers circuit is drawn around each partial. This yields Burgers vectors projected into the $(1\bar{1}0)$ plane of $\frac{1}{6}[\bar{1}\bar{1}2]$ [Fig. 8(a)] and $\frac{1}{12}[\bar{1}\bar{1}2]$ [Fig. 8(b)]. Assuming dislocations with minimal line energies, which implies minimal Burgers vectors, together with the position of the stacking fault, allows us to identify the two Burgers vectors to be $\boldsymbol{b}_1 = \frac{1}{6}[\bar{1}\bar{1}2]$ and $\boldsymbol{b}_2 = \frac{1}{6}[1\bar{2}1]$ (or $\boldsymbol{b}_2 = \frac{1}{6}[\bar{2}11]$), respectively. The geometry around the dislocation cores is resolved to that extent where it is possible to identify the partial dislocations. Hence, the line direction and projected Burgers vectors are known and the two dislocations are identified as 90° and 30° partial, respectively. The corresponding atomic structure is shown in Fig. 3 [(**4**), right panel], however, with a smaller stacking fault width.

From the contrast it was not possible to determine the exact position of the two core lines of the dislocation, probably since they are slightly kinked. Nevertheless, the stacking fault width could be estimated. For all investigated dislocations we find an estimated width of 3.10 ± 0.21 nm. This is very close to the results of the calculations presented in Sec. III, where 3.50 nm was predicted.

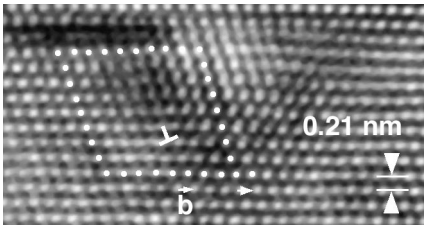

FIG. 9. Plan-view high-resolution electron microscopy image of an undissociated 60° dislocation in plastically deformed type IIa diamond after high-pressure, high-temperature annealing. The Burgers circuit is indicated.

Although most 60° dislocations are found to be dissociated, some appear to be undissociated, as shown in Fig. 9. The closure failure of the Burgers circuit in the HREM image determines the projected Burgers vector at $\frac{1}{4}[\bar{1}\bar{1}2]$ which corresponds to a perfect 60° dislocation. The atomic core structure of the undissociated 60° glide dislocation is shown in Fig. 3 [(**0**), right panel]. The observation of undissociated dislocations in plastically deformed diamonds is consistent with a barrier to dissociation as found above in Sec. III, or alternatively, to an impurity effect. No screw dislocations could be identified. However one has to keep in mind that in HREM only a small region of a sample can be imaged. Thus, the absence of screw dislocations in our images does *not* imply they do not exist in the investigated samples.

V. SUMMARY AND CONCLUSIONS

We have shown that dissociation of the 60° dislocation into a 30° and a 90° Shockley partial separated by a stacking fault is strongly favored from an energetic point of view. The dissociation, leading to a stacking fault width of 35 Å, produces an overall energy lowering of around 680 meV/Å. However, the first stages to the dissociation process reveal an energy barrier around 180 meV/Å. Such a barrier might explain the observation of some undissociated 60° dislocations in the HREM images. Most 60° dislocations are, however, dissociated with a stacking fault width around 30 Å.

These findings match well with our HREM experiments on natural brown diamond, where we find a majority of 60° dislocations dissociated into 30° and 90° Shockley partials, but some remaining undissociated.

Several possible core structures are examined for the screw $\frac{1}{2}[1\bar{1}0]$ dislocation. The three types: glide, shuffle, and mixed can be transformed into each other by the mere breaking and forming of bonds. The shuffle screw is found to be metastable, and around 860 meV/Å higher in energy than the glide structure. The latter resembles closely two 30° glide partials occupying the same Peierls valley. However, the bonds in the core are not completely reconstructed. The dissociation of this screw yields an energy drop of approximately 1 eV/Å. If the barrier to movement between Peierls valleys can be overcome, the screw dislocation will spontaneously dissociate.

Unfortunately, the HREM images failed to locate any

(dissociated) screw dislocations although we are unaware of any evidence for undissociated screws.

The glide of 90° and 30° partials has been considered in terms of processes involving kink formation and migration. Under these assumptions, the 90° glide dislocation proves to be the more mobile species, with a thermal activation energy of 3.5 eV for short dislocation segments. The migration barriers are on average 0.5 eV larger for the 30° glide partial while the double-kink formation energy exceeds that of the 90° partial even by 2 eV. Thus the resulting average thermal activation energy of the 30° glide partial is found to be $\overline{Q}_{30} \approx 6.1$ eV.

ACKNOWLEDGMENTS

Sample preparation was carried out by L. Rossou at EMAT. The experimental part of this work was performed within the framework of IUAP V-1 of the Flemish government.

*Electronic address: blumenau@phys.upb.de

[1] A.R. Lang, in *The Properties of Diamond*, edited by J.E. Field (Academic Press, London, 1982), p. 424.
[2] I. Kiflawi and A.R. Lang, Philos. Mag. **30**, 219 (1974).
[3] P.L. Hanley, I. Kiflawi, and A.R. Lang, Philos. Trans. R. Soc. London, Ser. A **284**, 329 (1977).
[4] N. Sumida and A.R. Lang, Philos. Mag. A **43**, 1277 (1981).
[5] J.W. Steeds, A.E. Mora, J.E. Butler, and K.M. Bussmann, Philos. Mag. A **82**, 1741 (2002).
[6] J.E. Graebner, M.E. Reiss, L. Seibles, T.M. Hartnett, R.P. Miller, and C.J. Robinson, Phys. Rev. B **50**, 3702 (1994).
[7] P. Humble and R.H.J. Hannink, Nature (London) **273**, 37 (1978).
[8] N. Sumida and A.R. Lang, in *Microscopy of Semiconducting materials*, edited by A.G. Cullis and D.C. Joy, IOP Conf. Proc. No. 60 (Institute of Physics, Bristol, London, 1981), p. 319.
[9] J.P. Hirth and J. Lothe, *Theory of Dislocations*, 2nd ed. (Wiley, New York, 1982).
[10] P. Pirouz, D.J.H. Cockayne, N. Sumida, S.P. Hirsch, and A.R. Lang, Philos. Trans. R. Soc. London, Ser. A **386**, 241 (1983).
[11] P.K. Sitch, R. Jones, S. Öberg, and M.I. Heggie, J. Phys. III **7**, 1381 (1997).
[12] R.W. Nunes, J. Bennetto, and D. Vanderbilt, Phys. Rev. B **58**, 12 563 (1998).
[13] X. Blase, K. Lin, A. Canning, S.G. Loui, and D.C. Chrzan, Phys. Rev. Lett. **84**, 5780 (2000).
[14] A.T. Blumenau, M.I. Heggie, C.J. Fall, R. Jones, and T. Frauenheim, Phys. Rev. B **65**, 205205 (2002).
[15] C.J. Fall, A.T. Blumenau, R. Jones, P.R. Briddon, T. Frauenheim, A. Gutiérrez-Sosa, U. Bangert, A.E. Mora, J.W. Steeds, and J.E. Butler, Phys. Rev. B **65**, 205206 (2002).
[16] J. Ruan, K. Kobashi, and W.J. Choyke, Appl. Phys. Lett. **60**, 3138 (1992).
[17] D. Takeuchi, H. Watanabe, S. Yamanaka, and H. Okushi, Phys. Rev. B **63**, 245328 (2001).
[18] A.T. Collins, H. Kanda, and H. Kitawaki, Diamond Relat. Mater. **9**, 113 (2000).
[19] D. Porezag, T. Frauenheim, T. Köhler, G. Seifert, and R. Kaschner, Phys. Rev. B **51**, 12947 (1995).
[20] T. Frauenheim, G. Seifert, M. Elstner, Z. Hajnal, G. Jungnickel, D. Porezag, S. Suhai, and R. Scholz, Phys. Status Solidi B **217**, 41 (2000).
[21] R. Jones and P.R. Briddon, in *Identification of Defects in Semiconductors*, edited by M. Stavola, Semiconductors and Semimetals, Vol. 51A (Academic Press, Bristol, Boston, MA, 1981), Chap. 6.
[22] P. Briddon and R. Jones, Phys. Status Solidi B **217**, 131 (2000).
[23] H. Koizumi, Y. Kammura, and T. Suzuki, Philos. Mag. A **80**, 609 (2000).
[24] F.R.N. Nabarro, Adv. Phys. **1**, 269 (1952).
[25] R.W. Nunes, J. Bennetto, and D. Vanderbilt, Phys. Rev. Lett. **77**, 1516 (1996).
[26] R.W. Nunes, J. Bennetto, and D. Vanderbilt, Phys. Rev. B **57**, 10388 (1998).
[27] M.I. Heggie, S. Jenkins, C.P. Ewels, P. Jemmer, R. Jones, and P.R. Briddon, J. Phys.: Condens. Matter **12**, 10263 (2000).
[28] W. Luyten, G. Van Tendeloo, and S. Amelinckx, Philos. Mag. A **66**, 901 (1992).
[29] B.E. Williams, H.S. Kong, and J.T. Glass, J. Mater. Res. **5**, 801 (1990).
[30] J. Narayan, J. Mater. Res. **5**, 2414 (1990).
[31] J.C. Angus, M. Sunkara, S.R. Sahaida, and J.T. Glass, J. Mater. Res. **7**, 3001 (1992).
[32] W. Marciniak, K. Fabisiak, S. Orzeszko, and F. Rozploch, J. Cryst. Growth **123**, 587 (1993).
[33] In cylindrical coordinates $\boldsymbol{r}=(R,\varphi,z)$ centered on the dislocation line, the displacement field is given as $\boldsymbol{u}(\boldsymbol{r})=(0,0,|\boldsymbol{b}_s|\varphi/(2\pi))$. Varying φ from 0 to 2π in a Burgers circuit then yields the correct Burgers vector in cylindrical coordinates $\boldsymbol{b}_s=(0,0,|\boldsymbol{b}_s|)$.
[34] The energy surface shown in Fig. 5 was obtained at 10×10 points in the two-dimensional parameter space by relaxing the whole structure subject to the constraint that the two primary atoms were constrained to lie in a plane perpendicular to the connecting line between the initial and final position. In the vicinity of **S**, the parameter mesh was refined by a factor of 10.